Astronomy & Astrophysics manuscript no. perri˙brandenburg˙2017
January 12, 2017
© ESO 2017

arXiv:1701.03018v1 [astro-ph.SR] 11 Jan 2017

Spontaneous flux concentrations from the negative effective magnetic pressure instability beneath a radiative stellar surface

B. Perri[1] and A. Brandenburg[2,3,4,5]

[1] DSM/IRFU/SAp, CEA-Saclay and UMR AIM, CEA-Université Paris 7, F-91191 Gif-sur-Yvette, France
[2] JILA and Department of Astrophysical and Planetary Sciences, University of Colorado, Boulder, CO 80303, USA
[3] Department of Astronomy, AlbaNova University Center, Stockholm University, 10691 Stockholm, Sweden
[4] Nordita, KTH Royal Institute of Technology and Stockholm University, 10691 Stockholm, Sweden
[5] Laboratory for Atmospheric and Space Physics, University of Colorado, Boulder, CO 80303, USA

January 12, 2017, Revision: 1.75

ABSTRACT

Context. The formation of sunspots requires the concentration of magnetic flux near the surface. The negative magnetic pressure instability (NEMPI) might be a possible mechanism for accomplishing this, but it has mainly been studied in simple systems using an isothermal equation of state without a natural free surface.
Aims. We study NEMPI in a stratified Cartesian mean-field model where turbulence effects are parameterized. We use an ideal equation of state and include radiation transport, which establishes selfconsistently a free surface.
Methods. We use a Kramers-type opacity with adjustable exponents chosen such that the deeper layers are approximately isentropic. No convection is therefore possible in this model, allowing us to study NEMPI with radiation in isolation. We restrict ourselves to two-dimensional models. We use artificially enhanced mean-field coefficients to allow NEMPI to develop, making it therefore possible to study the reason why it is much harder to excite in the presence of radiation.
Results. NEMPI yields moderately strong magnetic flux concentrations a certain distance beneath the surface where optical depth is unity. The instability is oscillatory and in the form of upward travelling waves. This seems to be a new effect that has not been found in earlier models without radiative transport. The horizontal wavelength is about ten times smaller than what has been found previously in more idealized isothermal models.
Conclusions. In our models, NEMPI saturates at field strengths too low to explain sunspots. Furthermore, the structures appear too narrow and too far beneath the surface to cause significant brightness variations at the radiative surface. We speculate that the failure to reproduce effects resembling sunspots may be related to the neglect of convection.

Key words. Radiative transfer – hydrodynamics – Sun: atmosphere – Sun: sunspots

1. Introduction

Sunspots are a highly intermittent manifestation of strong magnetic flux concentrations at the solar surface. The underlying magnetic fields are produced by hydromagnetic turbulence in the convection zone beneath the surface (Brun et al., 2004; Brown et al., 2011; Käpylä et al., 2012b; Augustson et al., 2015). Numerous simulations of turbulence and turbulent convection have displayed such magnetic field production by a dynamo process (Brandenburg and Subramanian, 2005). This alone, however, does not explain the occasional concentration into spots. On the other hand, more realistic simulations that include the effects of strong density stratification near the surface, as well as radiation and ionization, have been able to demonstrate the appearance of magnetic spots (Stein & Nordlund, 2012). Furthermore, it is known that strong density stratification can lead to a large-scale instability of an initially unstructured random magnetic field (Kleeorin et al., 1989, 1990). This instability leads to magnetic flux concentrations and even magnetic spots (Brandenburg et al., 2013; Warnecke et al., 2013) through the negative magnetic pressure instability (NEMPI). NEMPI has been associated with sunspot formation by Kleeorin et al. (1995, 1996), following a series of earlier work on its theoretical foundations (Kleeorin et al., 1993; Kleeorin and Rogachevskii, 1994; Rogachevskii & Kleeorin, 2007).

Numerical simulations have also displayed types of magnetic flux concentrations that are not straightforwardly associated with NEMPI. This tends to be the case when the magnetic field is produced by a large-scale dynamo some distance beneath the surface (Mitra et al., 2014; Jabbari et al., 2015, 2016). Nevertheless, also in those cases strong stratification was shown to be essential, as has been demonstrated by comparing with weakly stratified cases.

In the case of NEMPI, the underlying instability can well be modeled using mean-field magnetohydrodynamics, where the negative effective magnetic pressure is parameterized in terms of the mean magnetic field; see Brandenburg et al. (2016) for a review. In some of those cases there is good quantitative agreement between direct numerical simulations (DNS) and mean field simulations (MFS), as has been demonstrated in several papers (Kemel et al., 2013; Losada et al., 2013).

The main difference between MFS and DNS is the inclusion of the parameterization of the small-scale unresolved motions $\boldsymbol{u} = \boldsymbol{U} - \overline{\boldsymbol{U}}$ and magnetic fields $\boldsymbol{b} = \boldsymbol{B} - \overline{\boldsymbol{B}}$ in the MFS. Here, the overbar denotes a suitably defined average, which is in practice could be a spatial average. The evolu-

tion equations for $\overline{\boldsymbol{U}}$ involve correlations of the form $\overline{u_i u_j}$ and $\overline{b_i b_j}$ that need to be expressed in terms of $\overline{\boldsymbol{U}}$ and $\overline{\boldsymbol{B}}$. They are similar to the parameterization in terms of the rate-of-strain tensor of the mean flow involving turbulent viscosity, but there are also contributions that are quadratic in $\overline{\boldsymbol{B}}$. Similar parameterizations also exist for the Maxwell stresses in the momentum equation and the electromotive force in the induction equation.

Before we can think of applying NEMPI to real sunspot formation, we must begin to address the effects of radiation, ionization, and other potentially important surface effects. Here, we focus on radiative transfer. Radiation has two important effects. On the one hand, it leads to the establishment of a natural surface from which most of the observed radiation is emitted and above which the density drops off sharply. On the other hand, radiation also leads to the equilibration of temperature differences between neighboring fluid elements and reduces therefore all buoyancy effects, regardless of whether buoyancy is positive or negative. This has potentially detrimental effects on the instability that need to be assessed carefully. Earlier investigations have suggested that this may indeed be the case and that NEMPI may be difficult to excite in the presence of radiation (Barekat, 2013; Bhat & Brandenburg, 2016). This is also the reason why we focus here on mean-field simulations, because they allow us to artificially exaggerate the effects of NEMPI by choosing unrealistically large mean-field parameters, which allows us to study the properties of NEMPI in that case and helps us determining the conditions under which NEMPI may still operate.

Most of the earlier investigations of NEMPI have been carried out in an isothermally stratified layer using an isothermal equation of state. This means that no energy equation was solved. This was also true in simulations with an outer coronal envelope (Warnecke et al., 2013), where the interface was characterized by a layer above which the driving of turbulence was turned off. The aim of the present paper is therefore to study NEMPI in a simple model with radiative heating and cooling included.

2. The model

2.1. Mean-field equations and radiative transfer

We consider the mean-field equations in Cartesian coordinates, but restrict ourselves to including only the effects of turbulent magnetic diffusion, turbulent viscosity, and the negative effective magnetic pressure effect, which means that the ordinary magnetic pressure from the mean field, $\overline{\boldsymbol{B}}^2/2\mu_0$, is modified and becomes $(1-q_{\rm p})\overline{\boldsymbol{B}}^2/2\mu_0$, where $q_{\rm p}=q_{\rm p}(\overline{\boldsymbol{B}})$ depends on the local magnetic field strength. We write the mean magnetic field as $\overline{\boldsymbol{B}}=\boldsymbol{B}_0+\boldsymbol{\nabla}\times\overline{\boldsymbol{A}}$, where $\boldsymbol{B}_0=(0,0,B_0)$ is an imposed vertical field, and $\overline{\boldsymbol{A}}$ is the mean magnetic vector potential. We thus solve the equations for $\overline{\boldsymbol{A}}$, the mean velocity $\overline{\boldsymbol{U}}$, the mean specific entropy, $\overline{s}$, and the mean density $\overline{\rho}$ in the form

$$\frac{\partial\overline{\boldsymbol{A}}}{\partial t}=\overline{\boldsymbol{U}}\times\overline{\boldsymbol{B}}+\eta_{\rm T}\nabla^2\overline{\boldsymbol{A}}, \tag{1}$$

$$\overline{\rho}\frac{{\rm D}\overline{\boldsymbol{U}}}{{\rm D}t}=-\boldsymbol{\nabla}\left(\overline{P}-\frac{q_{\rm p}\overline{\boldsymbol{B}}^2}{2\mu_0}\right)+\overline{\boldsymbol{J}}\times\overline{\boldsymbol{B}}+\overline{\rho}\boldsymbol{g}+\boldsymbol{\nabla}\cdot(2\nu_{\rm T}\overline{\rho}\,\overline{\mathsf{S}}), \tag{2}$$

$$\overline{\rho}\,\overline{T}\frac{{\rm D}\overline{s}}{{\rm D}t}=-\boldsymbol{\nabla}\cdot(\boldsymbol{F}_{\rm rad}+\boldsymbol{F}_{\rm conv})+2\nu_{\rm T}\overline{\rho}\,\overline{\mathsf{S}}^2, \tag{3}$$

$$\frac{{\rm D}\ln\overline{\rho}}{{\rm D}t}=-\boldsymbol{\nabla}\cdot\overline{\boldsymbol{U}}, \tag{4}$$

where $\eta_{\rm T}=\eta+\eta_{\rm t}$ is the total magnetic diffusivity consisting of the sum of a microphysical and a turbulent value, $\nu_{\rm T}=\nu+\nu_{\rm t}$ is the total viscosity consisting again of the sum of a microphysical and a turbulent value, $\overline{\mathsf{S}}_{ij}=\frac{1}{2}(\overline{U}_{i,j}+\overline{U}_{j,i})-\frac{1}{3}\delta_{ij}\boldsymbol{\nabla}\cdot\overline{\boldsymbol{U}}$ is the traceless rate-of-strain tensor, $\overline{\boldsymbol{J}}=\boldsymbol{\nabla}\times\overline{\boldsymbol{B}}/\mu_0$ is the Lorentz force from the mean fields (without the effects of turbulence that are being parameterized through $q_{\rm p}$), $\boldsymbol{g}=(0,0,-g)$ is the gravitational acceleration, $\overline{P}$ is the mean gas pressure, $\overline{T}$ is the mean temperature, ${\rm D}/{\rm D}t=\partial/\partial t+\overline{\boldsymbol{U}}\cdot\boldsymbol{\nabla}$ is the advective derivative, $\boldsymbol{F}_{\rm rad}$ is the radiative flux, and $\boldsymbol{F}_{\rm conv}$ is the convective flux, but it will be neglected in our present exploratory work.

The radiative flux divergence is obtained by solving the radiative transfer equations for the intensity $I(\boldsymbol{x},t,\hat{\boldsymbol{n}})$ in the gray approximation in the form (Nordlund, 1982)

$$\hat{\boldsymbol{n}}\cdot\boldsymbol{\nabla}I=-\kappa\overline{\rho}\,(I-S) \tag{5}$$

along a set of rays in different directions $\hat{\boldsymbol{n}}$, where κ is the opacity and $S=(\sigma_{\rm SB}/\pi)\,\overline{T}^4$ is the source function with $\sigma_{\rm SB}$ being the Stefan–Boltzmann constant. The radiative flux divergence is found by integrating Equation (5) over all directions, i.e.,

$$\boldsymbol{\nabla}\cdot\boldsymbol{F}_{\rm rad}=-\kappa\overline{\rho}\oint_{4\pi}(I-S)\,{\rm d}\Omega, \tag{6}$$

We adopt the equation of state for a perfect gas, i.e., $\overline{P}=(\mathcal{R}/\mu)\overline{T}\,\overline{\rho}$, where $\mathcal{R}$ is the universal gas constant and μ the mean specific weight. The mean specific entropy is, up to an irrelevant additive constant, given by $\overline{s}/c_p=(\ln\overline{P})/\gamma-\ln\overline{\rho}$, where $\gamma=c_{\rm p}/c_{\rm v}$ is the ratio of specific heats at constant pressure and constant density, respectively, and $\mathcal{R}/\mu=c_{\rm p}-c_{\rm v}$. In the following we take $\gamma=5/3$, which is appropriate for a monatomic gas. The pressure scale height, $H_{\rm p}=-{\rm d}\ln\overline{P}/{\rm d}z$, is then given by $H_{\rm p}=\mathcal{R}\overline{T}/\mu g$. In the isothermal part near the top, pressure and density scale heights are equal, i.e., $H_\rho=H_{\rm p}$, where $H_\rho=-{\rm d}\ln\overline{\rho}/{\rm d}z$. However, in the deeper isentropic parts, we have $H_\rho=\gamma H_{\rm p}$.

2.2. Parameterizations

Turbulence effects such as NEMPI depend on the relative importance of the magnetic field to the equipartition field strength with respect to the turbulent energy, that is, on $\beta\equiv|\overline{\boldsymbol{B}}|/B_{\rm eq}$. Here, the equipartition field strength $B_{\rm eq}$ is given by $B_{\rm eq}^2(z)=\mu_0\overline{\rho}u_{\rm rms}^2$. The effective magnetic pressure is characterized by specifying the functional form of $q_{\rm p}=q_{\rm p}(\beta)$, for which we assume (Kemel et al., 2012)

$$q_{\rm p}(\beta)=\frac{q_{\rm p0}}{1+\beta^2/\beta_{\rm p}^2}=\frac{\beta_\star^2}{\beta_{\rm p}^2+\beta^2},\quad\text{where }\beta_\star=\beta_{\rm p}q_{\rm p0}^{1/2}. \tag{7}$$

In addition, we have to specify $\eta_{\rm T}$ and $\nu_{\rm T}$, which we assume to be constant and equal to each other, i.e., we assume the turbulent magnetic Prandtl number ${\rm Pr}_M=\nu_{\rm T}/\eta_{\rm T}$ to be unity (Yousef et al., 2003). We define a fiducial model

where we take $q_{\rm p0} = 300$ and $\beta_{\rm p} = 0.05$. Earlier work of Kemel et al. (2013) showed that the growth rate is mainly dependent on the parameter $\beta_\star$, whose value is then 0.87. For comparison, Kemel et al. (2012) and Käpylä et al. (2012a) used the parameter combination $q_{\rm p0} = 40$ and $\beta_{\rm p} = 0.05$, which then yields about a third for $\beta_\star = 0.32$. Our value of $\beta_\star$ is thus much higher than what has been assumed before, which should help us to study the effects of radiation in the development of NEMPI. Following earlier work of Barekat (2013) and Barekat & Brandenburg (2014), we assume a Kramers-like opacity law for κ of the form

$$\kappa = \kappa_0 (\overline{\rho}/\rho_0)^a (\overline{T}/T_0)^b \tag{8}$$

with constant coefficients κ_0, ρ_0, and T_0, and given exponents a and b. The resulting radiative conductivity is then given by (see Appendix A of Brandenburg, 2016)

$$K = K_0 \, \frac{(\overline{T}/T_0)^{3-b}}{(\overline{\rho}/\rho_0)^{1+a}} = K_0 \left[\frac{(\overline{T}/T_0)^n}{\overline{\rho}/\rho_0} \right]^{1+a}, \tag{9}$$

where $K_0 = 16\sigma_{\rm SB} T_0^3/3\kappa_0\rho_0$ is a constant and

$$n = (3-b)/(1+a) \tag{10}$$

is, under certain conditions, related to the polytropic index of the resulting stratification. The radiative diffusivity is $\chi = K/\overline{\rho} c_{\rm p}$. The optical depth is $\tau(z) = \int_z^\infty \kappa \overline{\rho} \, {\rm d}z'$. The region where $\tau \ll 1$ is optically thin, while the region where $\tau \gg 1$ is optically thick, which corresponds to the convection zone in the Sun; $\tau = 1$ represents thus the solar surface.

2.3. Boundary conditions and numerical aspects

We adopt impenetrable stress-free vertical field boundary conditions in the z direction, so the velocity obeys

$$\partial \overline{U}_x/\partial z = \partial \overline{U}_y/\partial z = \overline{U}_z = 0 \quad \text{on} \quad z = 0, \, L_z, \tag{11}$$

where L_z is the vertical extent of the computational domain. For the magnetic field we adopt the vertical field condition,

$$\partial \overline{A}_x/\partial z = \partial \overline{A}_y/\partial z = \overline{A}_z = 0 \quad \text{on} \quad z = 0, \, L_z. \tag{12}$$

We assume zero incoming intensity at the top, and compute the incoming intensity at the bottom from a quadratic Taylor expansion of the source function, which implies that the diffusion approximation is obeyed; see Appendix A of Heinemann et al. (2006) for details. As in Barekat & Brandenburg (2014), we fix temperature at the bottom,

$$\overline{T} = T_0 \quad \text{on } z = 0, \tag{13}$$

while the temperature at the top is allowed to evolve freely. There is no boundary condition on the density, but since no mass is flowing in or out, the volume-averaged density is automatically constant; see Appendix C of Barekat & Brandenburg (2014).

We solve Equations (1)–(6) on a two-dimensional mesh using either 288^2 or 576^2 meshpoints. We employ the Pencil Code[1], where all relevant terms are readily implemented. The code uses a high-order finite-difference scheme. The radiation module was implemented by Heinemann et al. (2006).

[1] https://github.com/pencil-code

Table 1. Units used in this paper and conversion into cgs units.

quantities	code units	cgs units
length $[z]$	Mm	10^8 cm
velocity $[u]$	$\mathrm{km\,s^{-1}}$	$10^5\,\mathrm{cm\,s^{-1}}$
time $[t]$, $[\lambda]^{-1}$	ks	10^3 s
density $[\rho]$	$\mathrm{g\,cm^{-3}}$	$1\,\mathrm{g\,cm^{-3}}$
temperature $[T]$	K	1 K
time $[t]$	ks	10^3 s
gravity $[g]$	$\mathrm{km^2\,s^{-2}\,Mm^{-1}}$	$10^2\,\mathrm{cm\,s^{-2}}$
opacity $[\kappa]$	$\mathrm{Mm^{-1}\,cm^3\,g^{-1}}$	$10^{-8}\,\mathrm{cm^2\,g^{-1}}$
diffusivity $[\chi, \eta_{\rm t}, \nu_{\rm t}]$	$\mathrm{Mm\,km\,s^{-1}}$	$10^{13}\,\mathrm{cm^2\,s^{-1}}$

2.4. Scale separation ratio

In our mean-field model, turbulence is parameterized in terms of a turbulent diffusivity, which is estimated to be $\eta_{\rm t} = u_{\rm rms}/3k_{\rm f}$ (Sur et al., 2008), where $k_{\rm f}$ is the wavenumber of the energy-carrying motions. We compare this with the smallest horizontal wavenumber $k_1 = 2\pi/L_z$ that fits into our domain of height L_z. We refer to $k_{\rm f}/k_1$ as the scale separation ratio. Thus, we have (Jabbari et al., 2014)

$$k_{\rm f}/k_1 = u_{\rm rms}/3\eta_{\rm t} k_1. \tag{14}$$

This ratio must be large enough for NEMPI to be excited (Brandenburg et al., 2012). Early DNS of Brandenburg et al. (2011), where NEMPI was excited, used $k_{\rm f}/k_1 = 15$, but with $k_{\rm f}/k_1 = 30$, NEMPI became much more pronounced (Käpylä et al., 2012a).

Following the work of Barekat & Brandenburg (2014), we choose $L_z = 5\,\mathrm{Mm}$. We adopt a squared domain, $L_x = L_z$, and assume for the turbulent small-scale velocity $u_{\rm rms} = 1\,\mathrm{km/s}$. Thus, we have $\eta_{\rm t} = 5\times10^{-3}\,\mathrm{Mm\,km/s}$, so we have $k_{\rm f}/k_1 = 53$, which should be large enough for NEMPI to be excited (Brandenburg et al., 2012). In some models with larger resolution (576^2 meshpoints), we used $\eta_{\rm t} = 2\times10^{-3}\,\mathrm{Mm\,km/s}$, corresponding to $k_{\rm f}/k_1 = 133$; see Table 1 for the conversion of several quantities from code units to cgs units. Following earlier work (Brandenburg et al., 2011), we also define the general turbulent–diffusive time $\tau_{\rm td} = (\eta_{\rm t} k_1^2)^{-1}$.

3. Results

We design the model such that it has an isentropic deeper part. The stratification in our model is similar to Run B7 of Barekat & Brandenburg (2014) with $a = 1$ and $b = 0$. This yields $n = 1.5$. In particular, we use $\kappa_0 = 10^7\,\mathrm{Mm^{-1}\,cm^3\,g^{-1}}$, which results in a surface temperature of around 5000 K; see Fig. 1 for a plot of the stratification of $\overline{\rho}(z)$, $\overline{s}(z)$, $\overline{T}(z)$, and $\chi(z)$. In the deeper parts, where $\tau \gg 1$, $\overline{T}$ increases linearly with depth and, because $\overline{s}$ is nearly constant, $\overline{\rho}(z) \propto \overline{T}^{3/2}$, which is in agreement with the expected polytropic stratification. Above the surface, $\overline{T}(z)$ is approximately constant, so $\overline{\rho}(z)$ falls off exponentially with height, as expected for an isothermal stratification. We begin by discussing in some detail a run with 200 G, which will later also be referred to as Run B″; see Table 2. The presence of an imposed field changes the stratification, but this change is small: T decreases by ≈ 4 K for $B_0 = 200$ G.

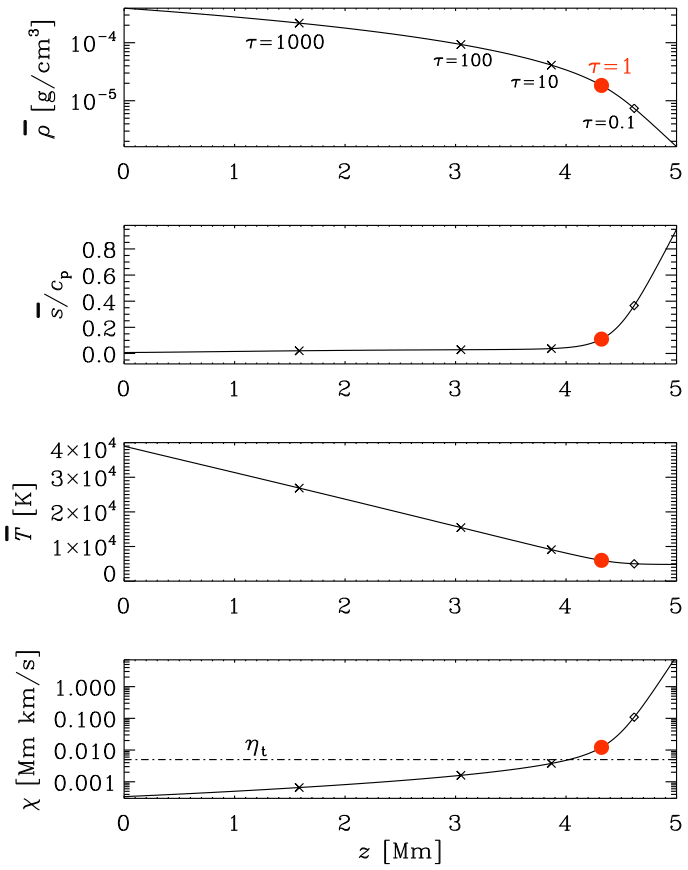

Fig. 1. Stratification of $\overline{\rho}$, $\overline{s}/c_{\rm p}$, $\overline{T}$, and χ. The location of $\tau = 1$ is marked with a red filled symbol, while the diamond indicates $\tau = 0.1$ and the two crosses denote $\tau = 10$ and 100. Here, $\kappa_0 = 10^7\,{\rm Mm}^{-1}\,{\rm cm}^3\,{\rm g}^{-1}$.

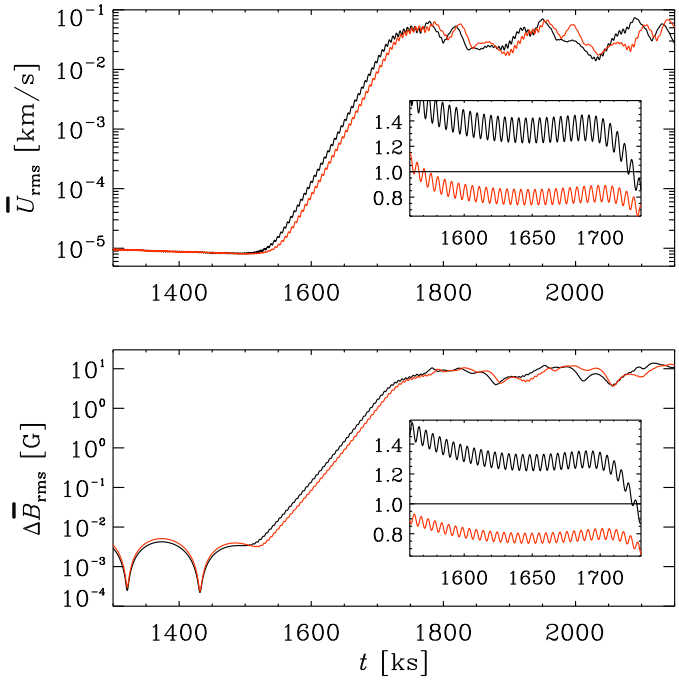

Fig. 2. Evolution of $\overline{U}_{\rm rms}$ and $\Delta\overline{B}_{\rm rms}$ for two runs with different initial seed magnetic field and $B_0 = 200\,{\rm G}$ in both cases. The insets show the compensated functions, $e^{-\lambda t}\overline{U}_{\rm rms}$ and $e^{-\lambda t}\Delta\overline{B}_{\rm rms}$, respectively, where λ is the growth rate. Only the short time interval of exponential growth is shown.

3.1. Early evolution into saturation

The growth of structures can be characterized both by the typical velocities $\overline{\boldsymbol{U}}$ in the domain and the departures from the imposed field $\Delta\overline{\boldsymbol{B}} = \overline{\boldsymbol{B}}_0 - \boldsymbol{B}_0$. In Fig. 2 we show for two independent realizations of Run B″ (so $L_x = L_z$) the evolution of the rms values, $\overline{U}_{\rm rms}$ and $\Delta\overline{B}_{\rm rms}$, with different seeds for the random initial velocity perturbations. We clearly see an oscillatory growth of both quantities, as can also be seen by showing a plot compensated by $\exp(-\lambda t)$, where $\lambda \approx 0.048\,{\rm ks}^{-1}$ is the growth rate, as determined during the exponential growth phase of the instability. In the following we measure the period $P_{\rm osc}$ as the volume-integrated rms velocity of the mean field and record the frequency $\omega = 2\pi/P_{\rm osc}$. The frequency of the actual (signed) magnetic field is half that value.

In the early phase of the evolution, structures form where $\max(|\overline{\boldsymbol{B}}|)$ is at $z = z_B \approx 2.5\,{\rm Mm}$ and a horizontal wavenumber $k = 4\,k_1$; see Fig. 3. These structures gradually move downward and new ones form, now at $z \approx 3\,{\rm Mm}$, which then also move down. The downward motions are associated with a local field enhancements, as can clearly be seen from field lines getting more concentrated in places. At later times the field becomes more irregular, but retains a typical horizontal wavenumber of $4\,k_1$. In some cases, however, we found that, in the late nonlinear stage, k can decrease from four to three.

The growth rate is independent of the initial seed for the random number generator, but the detailed nonlinear evolution does depend on it (compare the lines in each of the panels of Fig. 2). This suggests that the evolution of NEMPI is chaotic in the nonlinear regime. Animations show that the field lines are constantly swinging back and forth. This type of time-dependence of NEMPI is new and has not previously been seen – neither in isothermal nor polytropic calculations. It may therefore be an effect related to the presence of radiation. The slight apparent difference in os-

Table 2. Summary of Runs A–H.

	L_x	B_0	κ_0	$\eta_{\rm t}$	N	λ	ω	z_B
A	1.25	100	10^7	$5\,10^{-3}$	288^2	0.011	0.79	3.0
A′	2.5	100	10^7	$5\,10^{-3}$	288^2	0.009	0.89	2.5
B	1.25	200	10^7	$5\,10^{-3}$	288^2	0.030	1.44	2.7
B′	2.5	200	10^7	$5\,10^{-3}$	288^2	0.017	1.42	2.5
B″	5.0	200	10^7	$5\,10^{-3}$	288^2	0.049	1.21	2.5
C′	2.5	500	10^7	$5\,10^{-3}$	288^2	0.021	0.90	1.7
D	1.25	200	$2\,10^7$	$5\,10^{-3}$	288^2	0.022	1.51	2.8
E	1.25	200	$5\,10^7$	$5\,10^{-3}$	288^2	0.043	1.55	3.2
F	1.25	200	$2\,10^7$	$2\,10^{-3}$	576^2	0.094	0.70	2.7
G	1.25	200	$5\,10^7$	$2\,10^{-3}$	576^2	0.101	0.83	2.8
H	1.25	200	10^8	$2\,10^{-3}$	576^2	0.152	0.70	3.1

Notes. All quantities are measured in code units; see Table 1. In the first group of runs, B_0 is varied. In the second and third groups, κ_0 is varied, but in the third one, $\eta_{\rm t}$ is also decreased.

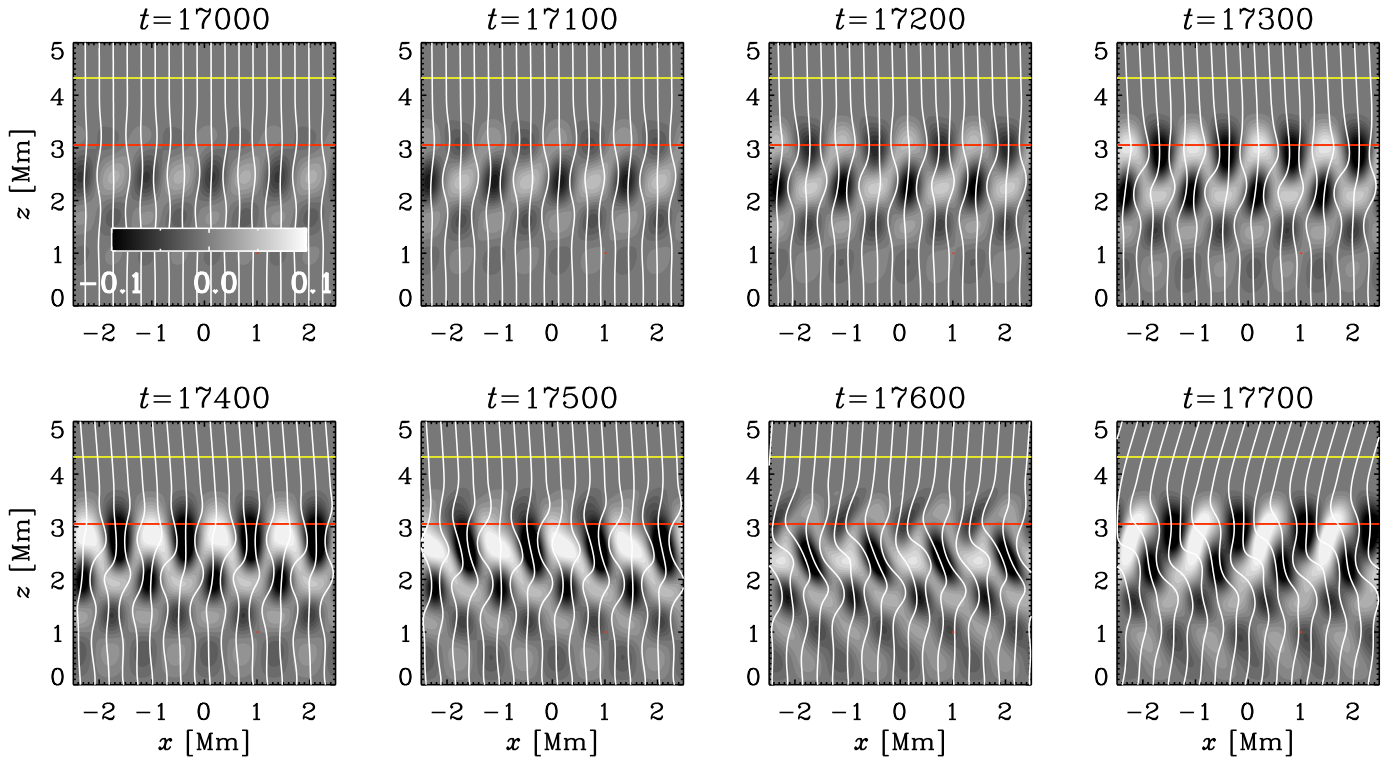

Fig. 3. Gray scale representation of vertical velocity together with magnetic field lines in white for a run with $B_0 = 200\,\mathrm{G}$ (Run B″). The yellow and red horizontal lines are the $\tau = 1$ and $\tau = 100$ surfaces, respectively,

cillation amplitudes of the compensated plots in the insets is caused by the fact that both have been compensated by the same factor, but the amplitudes were slightly different by the time the eigenfunction begins to be established.

The spatio-temporal evolution of NEMPI is seen more clearly in Fig. 4, where we show $\overline{U}_z(x_*, z, t)$ for $x_* = -1.7\,\mathrm{Mm}$. This position x_* is where $\overline{U}_z$ has an anti-node during the linear growth phase. At $t = 1740\,\mathrm{ks}$, the slope in the tz diagram corresponds to a pattern speed of about $0.2\,\mathrm{km\,s^{-1}}$, which is small compared with the sound speed $c_\mathrm{s} \approx 20\,\mathrm{km\,s^{-1}}$ at $z \approx 2.5\,\mathrm{Mm}$, and it is also small compared with the turbulent rms velocity of $1\,\mathrm{km\,s^{-1}}$, but it agrees with the typical NEMPI-produced downflow speeds found earlier for isothermal NEMPI experiments (Brandenburg et al., 2014).

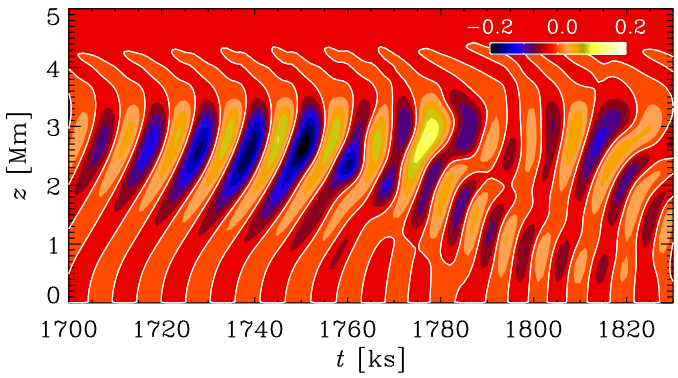

Fig. 4. $\overline{U}_z$ (color coded) versus t and z for Run B. The zero contours are shown in white.

3.2. Dependence on control parameters

We now consider the dependence of NEMPI on B_0, κ_0, and η_t. We revisit some of these dependencies later in more detail. Several input and output parameters of our runs are summarized in Table 2. Although most of the runs discussed in this paper are performed for a domain with $L_x = L_z = 5\,\mathrm{Mm}$, several aspects can also be reproduced in narrower domains with $L_x/L_z = 0.5$ and 0.25. The growth rate λ is rather sensitive to this, while the oscillation frequency $\omega = 2\pi/P_\mathrm{osc}$ and the position z_B of the magnetic field maximum are less sensitive. For Runs A–C with $\kappa_0 = 10^7\,\mathrm{Mm^{-1}\,cm^3\,g^{-1}}$, the growth rates are roughly in the range between $\lambda = 0.01\,\mathrm{ks^{-1}}$ and $0.03\,\mathrm{ks^{-1}}$ and do not seem to be systematically dependent on the value of B_0. This is mainly related to the fact that NEMPI can develop deeper down as B_0 is increased; see Kemel et al. (2012). This is characterized by the value of z_B given in Table 2; compare especially with the value for Run C. Our results thus confirm that the structures develop at larger depths when the field becomes stronger. This is in agreement with earlier work (Kemel et al., 2012; Losada et al., 2014).

3.3. Comparison with earlier work

In units of τ_td, the growth rate is $\tilde{\lambda} \equiv \lambda\tau_\mathrm{td} = \lambda/\eta_\mathrm{t}k_1^2$, which is about 6 for Run B″. However, if we normalize using instead the actual horizontal wavenumber k of the structures, which is 4 times larger than k_1 (see Fig. 3), we have in-

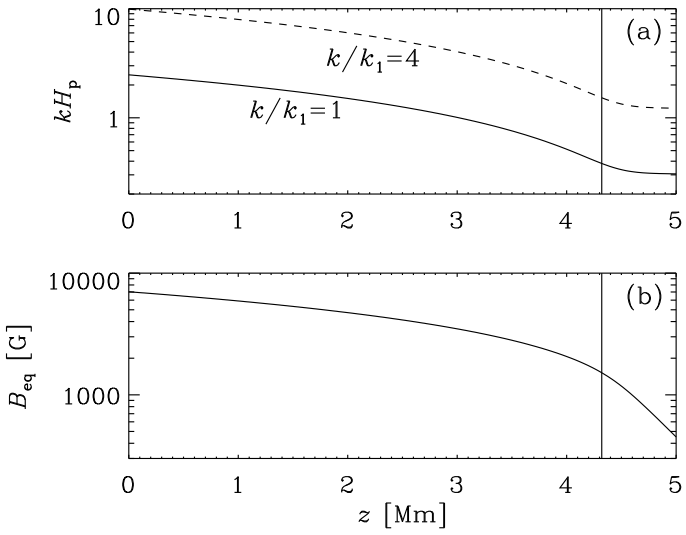

Fig. 5. Vertical dependence of kH_p for $k/k_1 = 1$ and 4 (a), and of B_{eq} (b). The vertical lines denote the surface where $\tau = 1$.

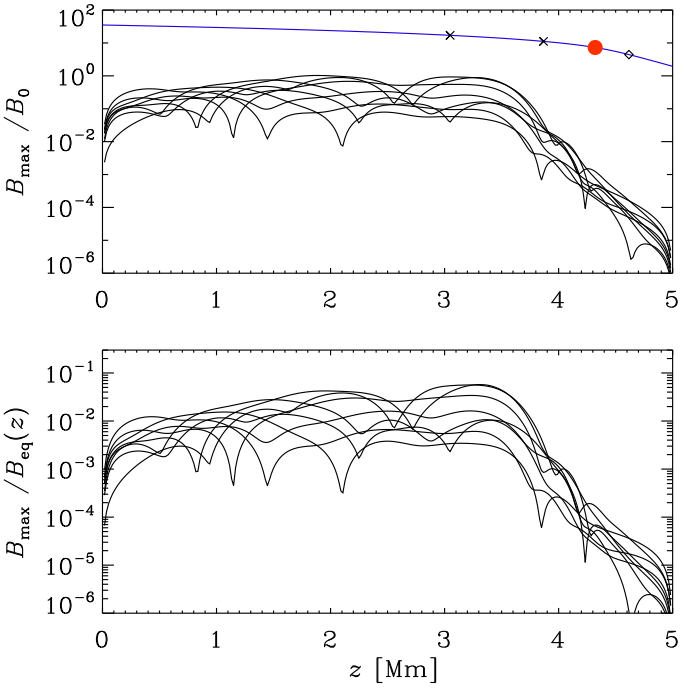

Fig. 6. Vertical dependence of the normalized magnetic field for different times in the nonlinear phase for $B_0 = 200\,\mathrm{G}$ (Run B″). The location of $\tau = 1$ is marked with a red filled symbol, while the diamond indicates $\tau = 0.1$ and the two crosses denote $\tau = 10$ and 100.

stead $\lambda/\eta_t k^2 \approx 0.4$. This value is rather low and comparable to the value in the first DNS of Brandenburg et al. (2011), where the scale separation ratio was much lower ($k_f/k_1 = 15$ compared to 53 in the present case).

Earlier work using isothermal layers has shown that the horizontal wavenumber of the instability is comparable to the inverse density scale height; Kemel et al. (2013) found $kH_\rho = 1.1$–1.5. Subsequent work showed that during the nonlinear evolution of the instability, kH_ρ can decrease from about 0.8 to 0.2. This has been associated with an inverse cascade-type behavior (Brandenburg et al., 2014). The polytropic simulations of Losada et al. (2014) gave larger values: $kH_\rho = 1$ in the upper layers and $kH_\rho = 2$ in deeper ones; see their Fig. 12. In the present case, at the height where the instability based on the absolute field strength is strongest ($z = 3\,\mathrm{Mm}$), and for $k/k_1 = 4$ we find $kH_p = 5$; see the dashed line in Fig. 5a. This is a striking difference between the present models and the earlier ones using an isothermal equation of state.

For large values of k, turbulent diffusive damping, which scales quadratically with k, becomes dominant. Thus, the instability is unable to develop large length scales. This is a clear reason for the growth rate of NEMPI being so strongly reduced in the present calculations when radiation transport is included. However, it is still unclear what causes kH_p to be so large in the presence of radiation.

Figure 5b shows that, in the region where NEMPI develops, the equipartition field strength $B_{eq}(z)$ is around 3000–4000 G. This is about 20 times larger than the strength of the imposed field, which is typical of NEMPI and in agreement with earlier results (Losada et al., 2014; Brandenburg et al., 2014).

3.4. Magnetic field dependence

As alluded to above, there are several aspects of NEMPI that can be compared with what has been found earlier. We now compare our results with Fig. 6 of Brandenburg et al. (2014), where the vertical dependence of the maximum field in the structures, $B_{max}(z)$, was plotted, normalized either by B_0 or by $B_{eq}(z)$. The corresponding result for our present simulations is shown in Fig. 6. The local maxima in $B_{max}(z)$ are caused by the spatial wave-like structures seen in Figs. 3 and 4.

Unlike the earlier work for isothermal layers, where the slope of B_{eq}/B_0 was constant, it varies in the present case. More importantly. the magnetic field drops significantly near the surface and does not cross the B_{eq}/B_0 line. This means that, unlike the earlier work with imposed vertical fields (Brandenburg et al., 2014), the field in the vertical flux tubes never exceeds B_{eq}.

The magnetic field strengths of the flux concentrations are obviously much weaker than what is expected for the Sun. More surprising is perhaps the fact that they are also much weaker than in the earlier isothermal models. For 200 G, the ratio B_{max}/B_0 reaches 1.1, while for 500 G, it reaches 0.94. In the isothermal case, this value could easily reach 50. We can also observe that, when we increase the external field, B_{max} becomes smaller.

3.5. Effective magnetic pressure

In Fig. 7 we plot the normalized effective magnetic pressure,

$$\mathcal{P}_{\rm eff}(\beta) = \tfrac{1}{2}[1 - q_p(\beta)]\beta^2, \qquad (15)$$

versus z. We compare this with Fig. 9 of Losada et al. (2014), which was a polytropic run with $\gamma = 5/3$. In the present work, the values of $\mathcal{P}_{\rm eff}$ are about ten times larger than in the earlier polytropic models. This is probably related to the rather large values of q_{p0} and $\beta_\star$. However, the shapes of the curves are similar in those two models.

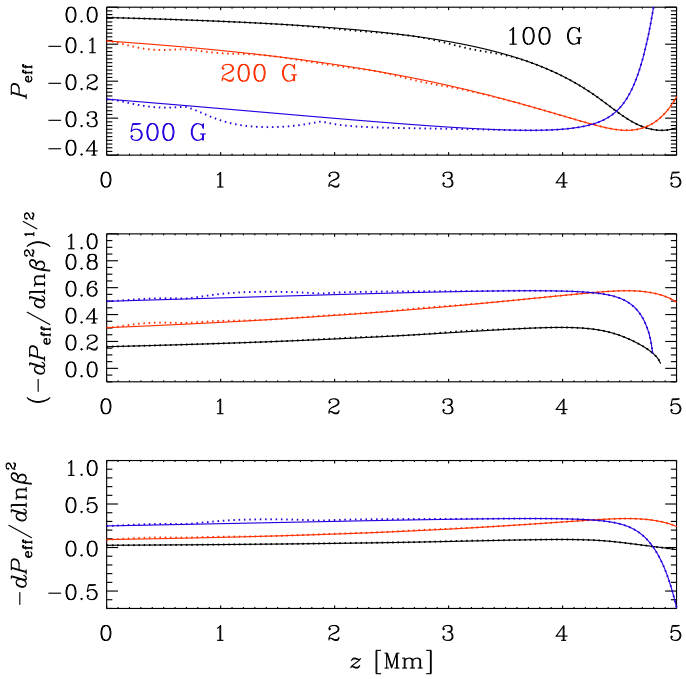

Fig. 7. Effective magnetic pressure and its derivative with respect to the magnetic field strength for $B_0 = 100\,\mathrm{G}$ (black), 200 G (red), and 500 G (blue), corresponding to $B_0/B_{\rm eq0} = 0.01$, 0.03, and 0.07. The solid lines are based on using just the imposed magnetic field, β_0, while the dotted lines are based on the actual field.

Our values of the relative strength of the imposed field are similar: for $B_0 = 200\,\mathrm{G}$ we have $B/B_{\rm eq} = 0.05$, which is comparable to the value of Losada et al. (2014). Our value of 100 G corresponds to their ratio 0.01, while 500 G corresponds to 0.07. The results change slightly when replacing $\beta_0 \equiv B_0/B_{\rm eq}$ by the value for the actual magnetic field $\beta = |\boldsymbol{B}|/B_{\rm eq}$. Furthermore, the changes in the magnetic pressure caused by the induced magnetic field are rather strong; see the dashed lines in Fig. 7. We also see regular variations in the vertical direction, which are associated with corresponding (time-dependent) extrema in the actual magnetic field.

3.6. Dependence on κ_0

Increasing κ_0 tends to let NEMPI appear sooner and grow faster. It also reduces the temperature near the top of the surface and therefore also the density scale height $H_{\rho 0}$.

To see whether radiation has a noticeable effect on NEMPI, we compare in Fig. 8 vertical profiles of the relative magnetic and temperature fluctuations $\langle\delta\ln\boldsymbol{B}^2\rangle^{1/2}$ and $\langle\delta\ln T\rangle$ for runs with different values of $\kappa_0 = 2\times10^7$, 5×10^7, and $10^8\,\mathrm{Mm}^{-1}\,\mathrm{cm}^3\,\mathrm{g}^{-1}$. The effect is surprisingly small. The magnetic fluctuations are of the order of unity (and somewhat larger for $\kappa_0 = 2\times10^7\,\mathrm{Mm}^{-1}\,\mathrm{cm}^3\,\mathrm{g}^{-1}$), while the relative temperature fluctuations are at most 5×10^{-4}.

The vigor of temporal variation of the field increases considerably as we increase κ_0, even though the relative strength of the variations and the effect on the temperature remain comparable.

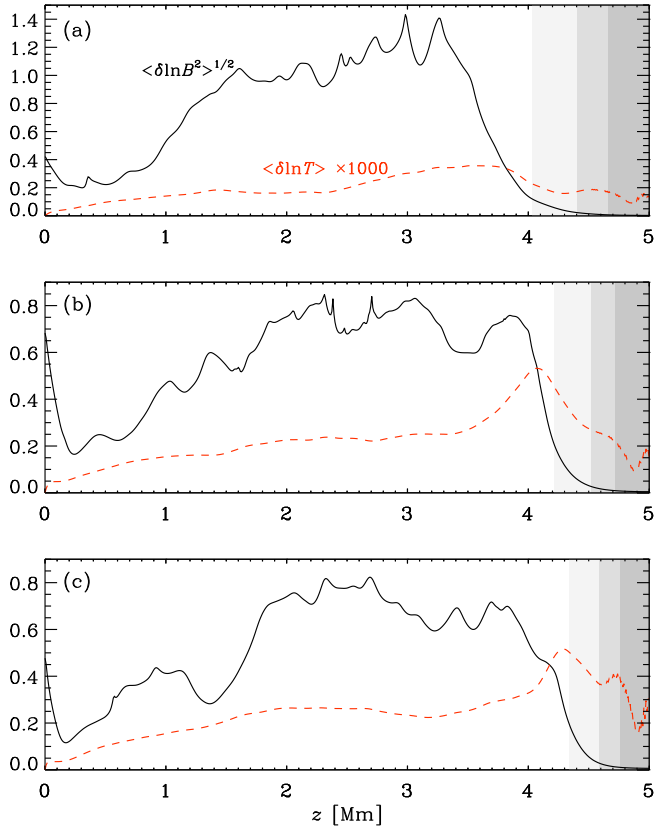

Fig. 8. Comparison of the vertical profiles of $\langle\delta\ln\boldsymbol{B}^2\rangle^{1/2}$ and $\langle\delta\ln T\rangle$ (scaled by a factor 1000) for runs with different values of $\kappa_0 = 2\times10^7\,\mathrm{Mm}^{-1}\,\mathrm{cm}^3\,\mathrm{g}^{-1}$ (a), 5×10^7 (b), and $10^8\,\mathrm{cm}^3\,\mathrm{s}^{-1}\,\mathrm{Mm}^{-1}$ (c). The $\tau = 10$, 1, and 0.1 surfaces are indicated in gray (from left to right).

3.7. Dependence on $q_{\rm p0}$ and $\beta_\star$

When the value of $q_{\rm p0}$ is below 250, keeping $\beta_{\rm p} = 0.05$ fixed, so $\beta_\star = 079$, NEMPI is found to be no longer excited and thus no magnetic structures are created. This remains true even when we increase κ_0 to $5\times10^7\,\mathrm{Mm}^{-1}\,\mathrm{cm}^3\,\mathrm{g}^{-1}$, which is generally more favorable to the onset of NEMPI. This may indicate that there is a threshold for $\beta_\star$ for the excitation of NEMPI in the presence of radiation, which would be somewhere between 0.7 and 0.8.

4. Conclusions

We have presented here the first calculations of NEMPI with radiation. Within the limitations of our simplified model, NEMPI would not have been excited had we chosen the previously determined control parameters for the negative effective magnetic pressure effect, i.e., $\beta_\star$ and $\beta_{\rm p}$. By using a nearly three times larger value of $\beta_\star$, we were able to study the reason behind this. It turned out that in our model with radiation, the horizontal wavelength of the instability is dramatically decreased. As a consequence, turbulent and radiative diffusion have much stronger effects, suppressing therefore the instability. Nevertheless, even with a strongly enhanced value of $\beta_\star$, the resulting magnetic structures are still far too weak to form sunspots.

We found for the first time that NEMPI can display oscillatory behavior during the linear phase of the instability. These oscillations are associated with travelling waves moving upward with a speed of $0.2\,\mathrm{km\,s^{-1}}$. The oscillations have a period of about 4–9 ks in the volume-integrated velocity, but since the period of the actual (signed) magnetic field is twice as long, so the recurrence time of pronounced downward flows is 8–18 ks.

We do not yet know enough about the nature of the oscillations and whether they could also exist in reality. To address this question further, we have to focus on the limitations associated with the small horizontal length scales of NEMPI in the presence of radiation.

The treatment of turbulent magnetic diffusion as a multiplicative factor in front of a Laplacian diffusion operator becomes invalid on small length scales, so the actual diffusion will be smaller; see Brandenburg et al. (2008). It is also possible that the opacity is still not large enough, and therefore the radiative diffusivity is too large. This is another unrealistic limitation of our present model. On the other hand, in the deeper layers, the radiative diffusivity is already now smaller than the turbulent magnetic diffusivity. One would therefore not have expected this to be the limiting factor. Most important is perhaps the limitation associated with the neglect of turbulent convection in the deeper parts. This would therefore be the first task to address in a future investigation.

Ultimately, the aim is to model the formation of sunspots, where convective heat transport is either suppressed by the magnetic field (Biermann, 1941) or the cooling enhanced (Parker, 1974a). The former effect may lead to its own instability, which was modelled by Kitchatinov & Mazur (2000) using a mean-field approach. This instability could be strengthened further by the effects of ionization and would therefore be another urgent target for subsequent investigations.

References

Augustson, K., Brun, A. S., Miesch, M., & Toomre, J. 2015, ApJ, 809, 149

Barekat, A. 2013, Hydrodynamic simulations with a radiative surface (Stockholm University, DiVA.org:su-90307)

Barekat, A., & Brandenburg, A. 2014, A&A, 571, A68

Bhat, P., & Brandenburg, A. 2016, A&A, 587, A90

Biermann, L. 1941, Vierteljahresschr. Astron. Gesellsch., 76, 194

Brandenburg A. 2016, ApJ, 832, 6

Brandenburg, A., & Subramanian, K. 2005, Phys. Rep., 417, 1

Brandenburg, A., Gressel, O., Jabbari, S., Kleeorin, N., & Rogachevskii, I. 2014, A&A, 562, A53

Brandenburg, A., Kemel, K., Kleeorin, N., Mitra, D., & Rogachevskii, I. 2011, ApJ, 740, L50

Brandenburg, A., Kemel, K., Kleeorin, N., & Rogachevskii, I. 2012, ApJ, 749, 179

Brandenburg, A., Kleeorin, N., & Rogachevskii, I. 2013, ApJ, 776, L23

Brandenburg, A., Rädler, K.-H., & Schrinner, M. 2008, A&A, 482, 739

Brandenburg, A., Rogachevskii, I., & Kleeorin, N. 2016, New J. Phys., in press, arXiv:1610.03459

Brown, B. P., Miesch, M. S., Browning, M. K., Brun, A. S., Toomre, J. 2011, ApJ, 731, 69

Brun, A. S., Miesch, M. S. & Toomre, J. 2004, ApJ, 614, 1073

Heinemann, T., Dobler, W., Nordlund, Å., & Brandenburg, A. 2006, A&A, 448, 731

Jabbari, S., Brandenburg, A., Losada, I. R., Kleeorin, N., & Rogachevskii, I. 2014, A&A, 568, A112

Jabbari, S., Brandenburg, A., Kleeorin, N., Mitra, D., & Rogachevskii, I. 2015, ApJ, 805, 166

Jabbari, S., Brandenburg, A., Mitra, D., Kleeorin, N., & Rogachevskii, I. 2016, MNRAS, 459, 4046

Käpylä, P. J., Brandenburg, A., Kleeorin, N., Mantere, M. J., & Rogachevskii, I. 2012a, MNRAS, 422, 2465

Käpylä, P. J., Mantere, M. J., & Brandenburg, A. 2012b, ApJ, 755, L22

Kemel, K., Brandenburg, A., Kleeorin, N., & Rogachevskii, I. 2012, Astron. Nachr., 333, 95

Kemel, K., Brandenburg, A., Kleeorin, N., Mitra, D., & Rogachevskii, I. 2013, Solar Phys., 287, 293

Kitchatinov, L. L., & Mazur, M. V. 2000, Solar Phys., 191, 325

Kleeorin, N., & Rogachevskii, I. 1994, Phys. Rev. E, 50, 2716

Kleeorin, N., Mond, M., & Rogachevskii, I. 1993, Phys. Fluids, 5, 4128

Kleeorin, N., Mond, M., & Rogachevskii, I. 1996, A&A, 307, 293

Kleeorin, N. I., Rogachevskii, I. V., & Ruzmaikin, A. A. 1989, Pis. Astron. Zh., 15, 639

Kleeorin, N. I., Rogachevskii, I. V., Ruzmaikin, A. A. 1990, Sov. Phys. JETP, 70, 878

Kleeorin, N., Rogachevskii, I., & Ruzmaikin, A. 1995, A&A, 297, 159

Losada, I. R., Brandenburg, A., Kleeorin, N., & Rogachevskii, I. 2013, A&A, 556, A83

Losada, I. R., Brandenburg, A., Kleeorin, N., & Rogachevskii, I. 2014, A&A, 564, A2

Mitra, D., Brandenburg, A., Kleeorin, N., Rogachevskii, I. 2014, MNRAS, 445, 761 769Intense bipolar structures from stratified helical dynamos

Nordlund, Å. 1982, A&A, 107, 1

Parker, E. N. 1974a, Solar Phys., 36, 249

Parker, E. N. 1974b, Solar Phys., 37, 127

Rogachevskii, I., & Kleeorin, N. 2007, Phys. Rev. E, 76, 056307

Stein, R. F., & Nordlund, Å. 2012, ApJ, 753, L13

Sur, S., Brandenburg, A., & Subramanian, K. 2008, MNRAS, 385, L15

Warnecke, J., Losada, I. R., Brandenburg, A., Kleeorin, N., & Rogachevskii, I. 2013, ApJ, 777, L37

Yousef, T. A., Brandenburg, A., & Rüdiger, G. 2003, A&A, 411, 321

$Header: /var/cvs/brandenb/tex/barbara/meanNEMPI/paper.tex,v 1.75 20